Acta Cryst. (1999). A**55**, 178–187

Experimental and theoretical characterization of structure in thin disordered films

D. G. McCulloch,[a]*† D. R. McKenzie,[a,b] C. M. Goringe,[a] D. J. H. Cockayne,[a] W. McBride[a] and D. C. Green[c]

[a]*Australian Key Centre for Microscopy and Microanalysis, University of Sydney, F09 NSW 2006, Australia,* [b]*School of Physics, University of Sydney, NSW 2006, Australia, and* [c]*Department of Applied Physics, UTS Broadway, NSW 2007, Australia. E-mail: dougal.mcculloch@rmit.edu.au*

(*Received 10 March 1998; accepted 24 June 1998*)

Dedicated to Professor A. F. Moodie on the occasion of his 75th birthday

Abstract

The electron microscope provides an ideal environment for the structural analysis of small volumes of amorphous and polycrystalline materials by enabling the collection of scattering information as a function of energy loss and momentum transfer. The scattered intensity at zero energy loss can be readily processed to a reduced density function, providing information on nearest-neighbour distances and bond angles. A method for collecting and processing the scattered intensity, which allows for the collection of an energy-loss spectrum for a range of momentum transfers, is discussed. A detailed structural determination from a reduced density function alone is difficult and it is shown that a more detailed structural model can be obtained by combining the experimental reduced density function with model structures obtained from molecular dynamics based on first-principles quantum mechanics. This method is applied to tetrahedral amorphous carbon, as an example of a monatomic network, and to aluminium nitride, as a prototype for a binary amorphous alloy.

1. Introduction

It was Alex Moodie and his colleagues, in their work on convergent-beam electron diffraction, who showed many of us that quantitative analysis of the scattered electron intensity as a function of momentum transfer is a powerful method for studying structures. This is also true for disordered or 'glassy' materials, which are of significant technological value. Of particular interest are the covalently bonded materials containing the light elements B, C, N, O and Al, some of which possess properties important for industrial applications. These materials are readily prepared in the form of thin films by physical vapour-deposition methods. Many of these materials have amorphous phases with a distinctive structure and properties that make them difficult to characterize. The most important structural issues are the degree of positional order (that is, whether the material is amorphous or nanophase crystalline) and for alloys the degree of site-occupancy order (that is, the extent of 'chemical' order).

Because the materials are usually prepared in the form of thin films, techniques that are capable of analysing small volumes, such as electron microscopy and electron diffraction, are valuable. The stoichiometry can be obtained by X-ray microanalysis or electron-energy-loss spectroscopy (EELS). Additional information can be obtained from the details in the core-loss edges in electron-energy-loss spectra. This latter information includes the electron-loss near-edge structure (ELNES), which occurs within approximately 50 eV of the edge onset and which probes atomic structure through the unoccupied low-lying electron states (Egerton, 1996). An example of the successful application of this method is the determination of hybridization states in amorphous carbon films (Berger *et al.*, 1988). The extended energy-loss fine structure (EXELFS), which occurs beyond about 50 eV from the edge onset, contains, in principle, sufficient information to determine the radial distribution function, $J(r)$, for the structure as viewed from an atom of each species present as the origin. In practice, EXELFS spectra are often limited in usefulness because of noise and therefore this method has been most successfully pursued with high-brightness X-ray sources in the technique known as extended X-ray absorption fine structure (EXAFS).

$J(r)$ is also readily accessible using energy-filtered elastic electron diffraction (Grigson, 1962; Graczyk & Moss, 1969). The collection of energy-filtered electron diffraction patterns and the conversion of these data into a radial distribution function have been shown to be useful for determining structural information such as nearest-neighbour distances and bond angles from a wide range of polycrystalline and amorphous materials. It is usually more convenient to use a related function $G(r)$, the reduced density function, defined in terms of $J(r)$ by

$$G(r) = [J(r)/r - 4\pi r\rho_0], \quad (1)$$

† Present address: Department of Applied Physics, RMIT, GPO Box 2476V, Melbourne 3001, Australia.

ISSN 0108-7673

where r is the interatomic distance and ρ_0 is the average density of the material. Previous work has seen the development of an experimental technique for the measurement of elastically scattered electron intensity from thin-film specimens and its conversion to $G(r)$ (Cockayne & McKenzie, 1988; Cockayne *et al.*, 1991). At the heart of the method is software for simultaneous control of the position of the electron diffraction pattern in the transmission electron microscope (TEM) at the plane containing the entrance aperture of the energy-loss spectrometer and the acquisition of the resulting signal as an electron-energy-loss spectrum. Energy-filtered diffraction has been used in the analysis of carbon allotropes [glassy carbon (McKenzie, Green *et al.*, 1990), tetrahedral amorphous carbon (ta-C) (McKenzie *et al.*, 1991) and C_{70} (McKenzie *et al.*, 1992)], carbon nitride (Merchant *et al.*, 1996), boron nitride (McKenzie, Sainty & Green, 1990) and electronic materials such as SiC:H (Sproul *et al.*, 1986).

A major limitation to the use of $G(r)$ for characterization of amorphous solids arises from the fact that, for electron diffraction, the $G(r)$ measured is a combination of all the partial radial distribution functions for each species in the solid. In addition, although it is true that under some conditions a unique structural model that reproduces the scattered intensity for all momentum transfers can be determined (Evans, 1990), in practice, where the diffracted intensity is only known over a limited range of momentum transfers, there will be many qualitatively different models that will equally well fit the data. In this work, we show how the accurate modelling of structure using first-principles quantum-mechanical molecular dynamics can be used to overcome these difficulties. The key component of this modelling approach is the use of density functional theory to calculate interatomic forces. This method is based on a very general quantum-mechanical description of the bonding electrons which gives it great predictive power with a minimum of adjustable parameters. When combined with experimental studies, this technique has proved extremely powerful in solving structural problems in chemistry, biology and physics. For example, the technique has recently been used to study systems as complex as a hydrated RNA duplex (Hutter *et al.*, 1996), and the binary tetrahedral solids SiO_2 (Sarnthein *et al.*, 1995) and $GeSe_2$ (Cobb *et al.*, 1996).

In this paper, we first review the collection of energy-filtered diffraction patterns in the transmission electron microscope and the processing of these data to obtain $G(r)$. Then the application of accurate atomistic modelling for determining possible structural arrangements to compare with the experimentally determined $G(r)$ is discussed. This modelled structure is then used as the starting point for further refinement using a procedure based on the so-called reverse Monte Carlo method (McGreevy & Howe, 1992). It is shown that it is important to have a realistic starting structure since the reverse Monte Carlo method is open to the possibility of generating a false structure with coincidental agreement with the experimental $G(r)$. The refined structure is accepted as the best structural model provided that it lies close to the minimum energy of the theoretical structure. To illustrate the advantages of a combined experimental and theoretical modelling approach, the examples of cathodic arc deposited tetrahedral amorphous carbon and aluminium nitride are presented.

2. Experimental

2.1. *Materials synthesis*

Materials in the form of thin films were deposited in a cathodic arc (Aksenov *et al.*, 1978). In this method, a high-temperature plasma is created on the surface of the source material by means of an arc operating at a current of order 100 A. The plasma creates a highly ionized plasma stream consisting of ions and electrons. This stream is filtered magnetically to remove neutrals and macroscopic particles, and is condensed onto a substrate at room temperature. The quenching rate in such a method is very high and is dependent to some extent on the thermal contact between the growing surface and a thermal sink. In the case of carbon, a graphitic target is used. The amorphous tetrahedral form of carbon occurs when the quench rate is high and a considerable compressive stress is incorporated into the film. In the case of aluminium nitride, an aluminium target is used and a nitrogen background gas acts as the source of nitrogen. The quench rate is important here also, and specimens with the finest crystal size are produced when the deposition rate is low, producing a small temperature gradient between the growing film and the thermal sink and hence a high quench rate.

2.2. *Instrumentation*

A technique for the collection of energy-filtered electron diffraction patterns in a TEM, and their conversion to $G(r)$, has been reported previously (Cockayne & McKenzie, 1988). In that technique, the diffracted intensity $I(s, \Delta E)$ is collected for a range of momentum transfers s [where $s = 2\sin(\theta)/\lambda$], and for a fixed value of electron-energy loss ΔE (zero for elastic scattering), resulting in an energy-selected diffraction pattern for a particular ΔE. The technique has been extended to the collection of the diffracted intensity for a range of s and a range of ΔE by collecting a series of energy-loss spectra $I(\Delta E)$ for a series of momentum transfers s. From this set of spectra, the diffraction pattern can be constructed for any value of ΔE. Further, $I(s, \Delta E)$ can be studied as a three-dimensional set and the dispersion of spectral features with momentum transfer can be studied.

All spectra were collected using a GATAN 666 parallel EELS (PEELS) detection system on a Philips EM430 TEM operating in selected-area diffraction mode at a voltage of 300 kV. The experimental arrangement has been outlined previously (Cockayne *et al.*, 1991) and a schematic diagram is shown in Fig. 1. The procedure used to collect energy-loss information as a function of scattering angle is controlled by a 'custom function' executed from within the Gatan *EL/P* software program, enabling it to act as a multichannel analyser for data collection and processing.

The diffraction pattern is scanned across the PEELS entrance aperture by means of a digitally incremented signal applied to the post-specimen scan coils of the TEM. The problem of detector saturation as the central spot is passed over the entrance aperture has been solved by deflecting the electron beam away from the photodiode array while moving through this region of the diffraction pattern, using the voltage scan module (VSM) to apply an accurately calibrated voltage to the spectrometer drift tube.

The value of momentum-transfer increment Δs is determined by collecting a diffraction pattern from a standard specimen, usually in the form of a thin metal film (Al or Pt). During this calibration procedure, it is essential that the microscope-lens settings be kept identical to those used when collecting data from the specimen of interest. Typically, $\Delta s \approx 0.003$ Å^{-1}.

The procedures for the data collection reported previously (Cockayne *et al.*, 1991) have been modified as follows. The spectral region saved at each scattering angle is an energy window around the zero-loss peak (ZLP). For the collection of zero-loss diffraction intensities, this spectral region is typically 50 channels wide. However, a spectrum from a larger user-defined energy window can also be saved at each value of s, for example to allow the study of the dispersion of plasmons. Following the collection of each spectrum, the position of the ZLP is determined using a peak-search routine. Any drift is then corrected using the VSM. This ensures that each spectrum is collected using the same region of the photodiode array, eliminating the need to correct for diode-to-diode gain variations. In order to minimize the so-called 'memory effect' caused by the incomplete recharging of the photodiode array between collections, a number of clear-out or 'dummy' spectra are collected between each saved spectrum with the ZLP shifted well away from the diode array using the VSM.

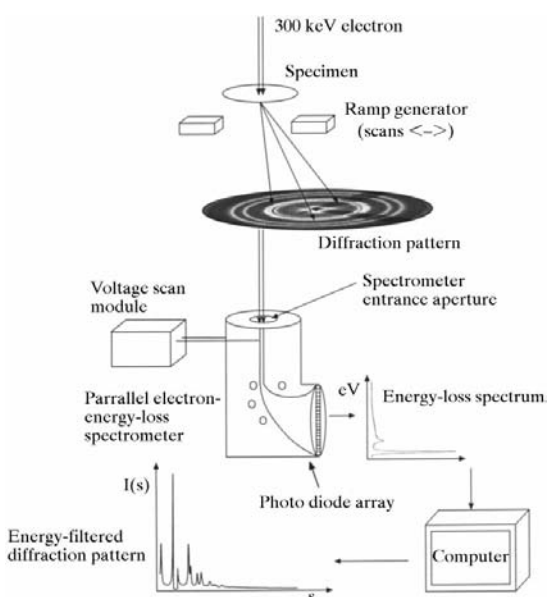

Fig. 1. A schematic diagram of the experimental set-up for the collection of the energy-loss data as a function of momentum transfer in a transmission electron microscope.

All data analysis, such as the determination of the diffracted electron intensity at each scattering angle, is conducted off-line using a second program. This is important in the case of energy-filtered diffraction-pattern collection where instrumental drift in the TEM, such as changes in illumination intensity, will complicate the measurement of the relative electron intensity at each scattering angle. The above procedure can collect 800–1000 points or channels of data (*e.g.* from $s = 0$ to $s = 4$ Å^{-1} with $\Delta s \approx 0.003$ Å^{-1}) in approximately 30 min.

2.3. *Collection of energy-filtered electron diffraction patterns (EFDP)*

Fig. 2 shows the typical output following the off-line processing of data collected using the above procedure. In order to minimize the effects of incomplete recharging of the photodiode array, three spectra were collected and discarded between each saved spectrum. At each channel (corresponding to different scattering angles), the elastic scattered intensity is then calculated (Fig. 2*a*). In addition to the intensity of elastic scattering, other information such as the integration time (Fig. 2*b*), background level (Fig. 2*c*) and the position of the zero-loss peak on the diode array (Fig. 2*d*) can be obtained at each channel. Owing to the limited dynamic range of the photodiode array, the integration time must be changed several times during the collection to ensure that data with good signal-to-background ratio are collected at all scattering angles. The background level is determined by averaging the counts in an energy window 24 channels wide, located to the low-energy side of the ZLP. This background level is due to the dark current from the photodiodes in the detector, and its contribution to the measured signal is dependent on the temperature of the photodiode array. Since the background is measured for each spectrum collected, any variation in the detector background during the collection of an EFDP can be accounted for. The position of the ZLP on the photodiode array is a sensitive measure of the experimental

conditions and can be used to monitor instrument stability during data collection.

At large scattering angles, the scattering intensity becomes small compared with the detector noise and it is difficult to reliably measure the ZLP intensity. An alternative method involves the integration of the positive portion of the ZLP after the application of a smoothed second difference filter. The smoothed second difference filter is employed to help extract the zero-loss peak intensity from strong plasmons at small scattering angles and from noisy backgrounds at high scattering angles. Since the entire spectrum around the ZLP is saved at each channel, various methods for calculating the elastic scattered intensity can be tested off-line.

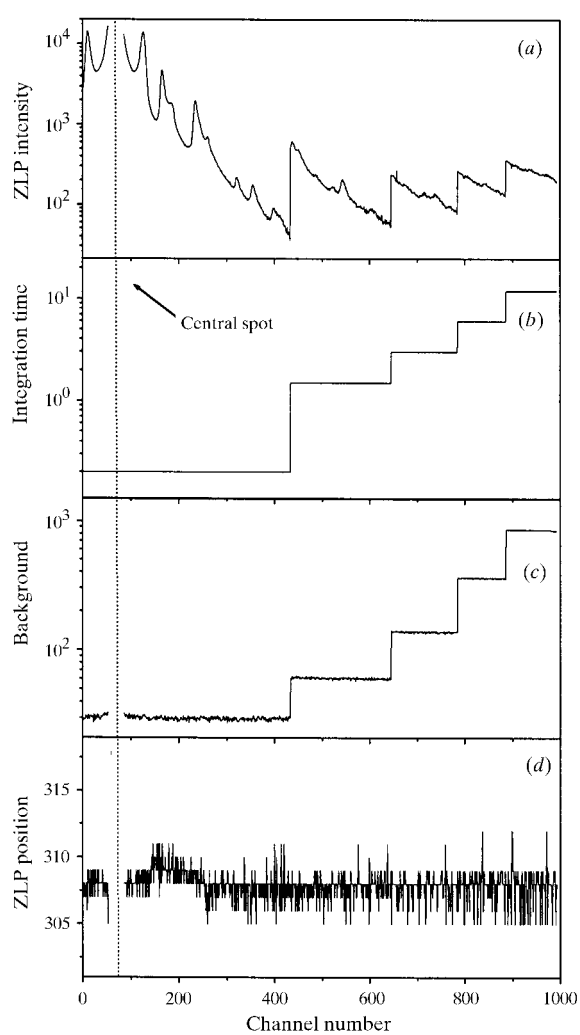

Fig. 2. Typical output following the off-line processing of the energy-loss data as a function of momentum transfer into an energy-filtered diffraction pattern. (*a*) Elastic scattering intensity; (*b*) integration time; (*c*) average background level; (*d*) location of the zero-loss peak on the diode array.

2.4. *Collection of plasmon dispersion data*

As discussed above, the collection procedure stores an energy-loss spectrum at each scattering angle. This enables the plasmon-loss features to be studied as a function of momentum transfer – a study known as plasmon-dispersion analysis. Fig. 3 shows an example of plasmon dispersion for energy-loss range 0 and 50 eV and for momentum transfers in the range 1.4 and 2.2 Å^{-1} for aluminium. In a recent paper, we report the use of this technique to investigate the plasmon-dispersion behaviour of various carbon-based materials (McBride *et al.*, 1998).

3. Theoretical considerations

3.1. *Calculation of the reduced density function G(r)*

The experimentally collected elastic scattering intensities are first converted into an accurately calibrated EFDP, $I(s)$, following the procedures reported earlier (Cockayne & McKenzie, 1988; Cockayne *et al.*, 1991). This processing occurs in several steps including correction for integration times, determining the centre of the diffraction pattern, and calibrating the angular scale.

The EFDP contains information on the elastically scattered component of the diffraction pattern, which is due to the structural arrangements of atoms in the specimen, and can be transformed into $G(r)$ using a Fourier sine transform to give real-space information about the material. For a single element, this inter-relationship can be summarized (for more details see Cockayne & McKenzie, 1988) as:

$$I(s) \overset{\text{modify}}{\longrightarrow} \varphi(s) = \frac{I(s) - Nf(s)^2}{Nf(s)^2} s$$

$$\overset{\text{transform}}{\longrightarrow} G(r) = 4\pi r[\rho(r) - \rho_0]. \qquad (2)$$

$\varphi(s)$ is known as the reduced intensity function, $f(s)$ is the atomic scattering factor for electrons for a specific element and is evaluated from tabulated values (Doyle

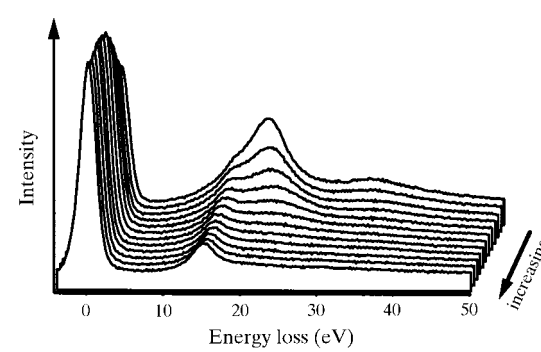

Fig. 3. A selection of energy-loss spectra with different momentum transfers for the energy range 0–50 eV. Such data can be used to study plasmon-loss features as a function of momentum transfer.

& Turner, 1968) and N is a scaling factor related to the number of atoms contributing to the diffraction pattern. The variables r, $\rho(r)$, ρ_0 are the interatomic distance, local number density of atoms and bulk number density, respectively. In the case of a material containing more than one kind of atom, a useful approximation is to replace $f(s)$ by the weighted average scattering factor. This approximation assumes the scattering factors are multiples of each other and will be used in this paper. $G(r)$ is then an average radial distribution function showing peaks at interatomic distances with a size-dependent number of atoms involved.

3.2. *Theoretical modelling*

Molecular-dynamics methods based on accurate calculation of interatomic forces from first principles provide an insight into the structure of amorphous networks at a level that is difficult, if not impossible, to obtain from currently available experimental methods. The most accurate generally available methods for obtaining interatomic forces in extended systems are based on density functional theory (Hohenberg & Kohn, 1964; Kohn & Sham, 1965) in the generalized gradient approximation. We show that the predictions of molecular dynamics used in conjunction with experimentally obtained information are a powerful combination for structural analysis.

The implementation of density functional theory used is the *Car–Parrinello molecular-dynamics* (CPMD) method (Car & Parrinello, 1985). This method uses a plane-wave basis set to describe the wavefunctions of valence electrons, with the core electrons and atomic cores being incorporated in the form of pseudopotentials.

In the Car–Parrinello technique, classical molecular dynamics of the atomic cores is combined with fictitious molecular dynamics for the electrons, with the expansion coefficients of the electron wavefunctions used as the coordinate set. The expansion coefficients evolve in such a way as to keep the system close to the minimum energy or *Born–Oppenheimer* surface at all times. The Car–Parrinello method is distinguished from other quantum-molecular-dynamics implementations in that the atomic coordinates and electronic expansion coefficients evolve simultaneously.

The simulations performed in this work closely follow the procedure described previously (Marks *et al.*, 1996) for tetrahedral amorphous carbon, in which a cell of 64 atoms at a density of 2.9 g cm^{-3} and a plane-wave energy cutoff of 476.2 eV was used. This procedure involved the formation of a pseudoliquid followed by a rapid quench (the liquid-quench method). The liquid-quench method simulates the so called 'thermal spike', which occurs during film formation by energetic condensation processes. In the present work, tetrahedral amorphous carbon is simulated using a larger cell containing 125 atoms and a plane-wave energy cutoff of 544.2 eV, which allows a more extensive comparison with experiment to be made. A second simulation was performed for amorphous AlN using a cell containing 32 N and 32 Al atoms with a plane-wave energy cutoff of 680.3 eV. Both simulations were performed at a density of 2.9 g cm^{-3} and with the BLYP (Becke, 1988; Lee *et al.*, 1988) representation of the exchange and correlation potential. Periodic boundary conditions were applied in all three directions. The atoms were initially placed in a simple cubic structure. When the molecular dynamics run was started, this high-energy structure rapidly melted and the temperature of the system rose to over 5000 K. The system was coupled to a heat bath by means of a Nose–Hoover (Nose, 1984; Hoover, 1985) thermostat and annealed at 4000 K for 350 fs. The final structure was formed by quenching to 300 K over a period of 500 fs.

At the completion of the molecular dynamics simulation, the structure was further refined by a procedure based upon the reverse Monte Carlo method (McGreevy & Howe, 1992). $\varphi(s)_{\rm theory}$ for the theoretical structure was generated from the Debye formula, summed over all bonds of length r:

$$\varphi(s)_{\rm theory} = \sum_{\rm bonds} \sin(2\pi rs)/2\pi rs. \qquad (3)$$

The mismatch between the theoretical and experimental $\varphi(s)_{\rm expt}$ is assessed by

$$\chi^2 = \sum_s [\varphi(s)_{\rm theory} - \varphi(s)_{\rm expt}]^2/\sigma(s)^2, \qquad (4)$$

where the experimental uncertainty, $\sigma(s)$, was estimated from the noise in the experimental data.

This mismatch was then reduced by means of imposing random variations on the structure as follows. At each step, a trial set of new atomic coordinates was created by adding or subtracting random values, of the order of 0.01 Å, to each coordinate. The new set of coordinates was accepted if it resulted in a reduction of χ^2; if the result was an increase in χ^2 then the new coordinates were accepted with a probability

$$\exp[-(\chi^2_{\rm new} - \chi^2_{\rm old})/2]. \qquad (5)$$

A few thousand such random changes were required to reduce χ^2 to its asymptotic value.

4. Results and discussion

4.1. *G(r) analysis of glassy carbon*

To illustrate the procedures involved in obtaining a $G(r)$ from an energy-filtered diffraction pattern, the example of glassy carbon (a turbostratic form of graphite) is employed. Glassy carbon is a type of synthetic graphite produced by the pyrolysis of highly cross linked polymers. X-ray diffraction experiments have revealed that the microstructure of glassy carbon

consists of carbon atoms bonded predominantly in graphite-like planes (Jenkins & Kawamura, 1976). The registration of a graphitic plane with respect to its neighbouring planes is poor however. Therefore, the $G(r)$ of glassy carbon should contain only peaks corresponding to the in-plane distances in graphite, and this provides a good evaluation of the method.

Fig. 4(a) shows a calibrated experimental $I(s)$ from glassy carbon heat-treated to 2770 K, computed using a smooth second difference filter. Also shown is the fit to $Nf(s)^2$, which displays good agreement with $s = 3.7$ Å^{-1}. The resulting $\varphi(s)$ is shown in Fig. 4(b). Owing to noise in $I(s)$ at high s, it is usually necessary to apply a damping factor $\exp(-Bs^2)$ to $\varphi(s)$ to reduce the effects of this noise, which otherwise can produce ripple in $G(r)$. The resulting $G(r)$ for glassy carbon calculated using a Fourier sine transform of the $\varphi(s)$ shown in Fig. 4(b) is plotted in Fig. 5(a). The three nearest neighbours are found to be at 1.42, 2.44 and 3.75 Å, respectively (indicated in the figure). As expected, these distances correspond to the first three nearest neighbours in a graphite sheet and are expected in glassy carbon, which, as discussed above, is known to have good in-plane graphitic order. Also apparent is the lack of any distances corresponding to interplanar correlations.

4.2. *Tetrahedral amorphous carbon*

Tetrahedral amorphous carbon (ta-C) is a dense form of amorphous carbon with a predominance of atoms in sp^3 bonding configurations formed using energetic condensation methods (McKenzie *et al.*, 1991). It is of interest as a hard coating and has interesting electronic properties. Fig. 5(b) shows the $G(r)$ obtained from cathodic arc deposited tetrahedral amorphous carbon. The first-nearest-neighbour peak occurs at 1.52 Å, which is larger than that observed in glassy carbon owing to the high sp^3 fraction in tetrahedral amorphous carbon (Berger *et al.*, 1988). Owing to the amorphous nature of the bonding in ta-C, the $G(r)$ is more difficult to interpret than it is for glassy carbon as well defined distances are less discernible.

To compare the theoretically derived structure with the experiment results, Fig. 6(a) shows a snapshot of the 125-atom carbon network structure determined using the Car–Parrinello simulations described in §3.2. The features present are generally similar to those reported previously by Marks *et al.* (1996) for a smaller simulation cell containing 64 atoms. In particular, three- and four-membered carbon rings are present and 60% of the atoms are sp^3 bonded. The three- and four-membered

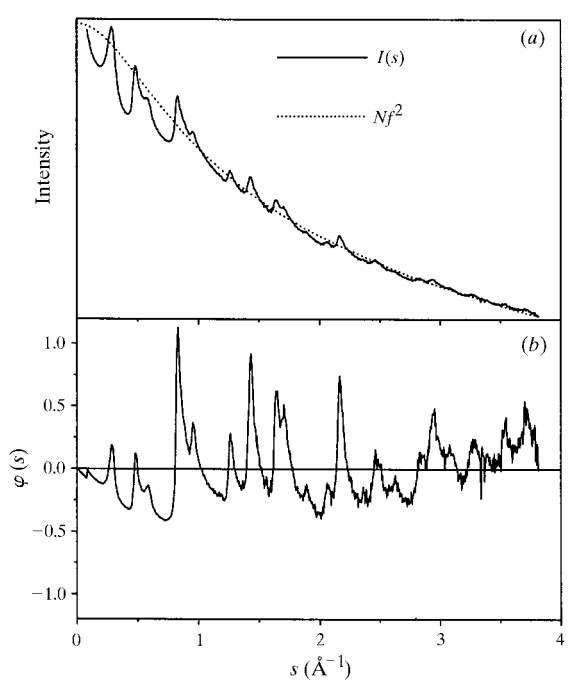

Fig. 4. The process of calculating $\varphi(s)$ from an energy-filtered diffraction pattern of glassy carbon. (a) Fit of $Nf(s)^2$ to the experimental $I(s)$; (b) the resulting $\varphi(s)$.

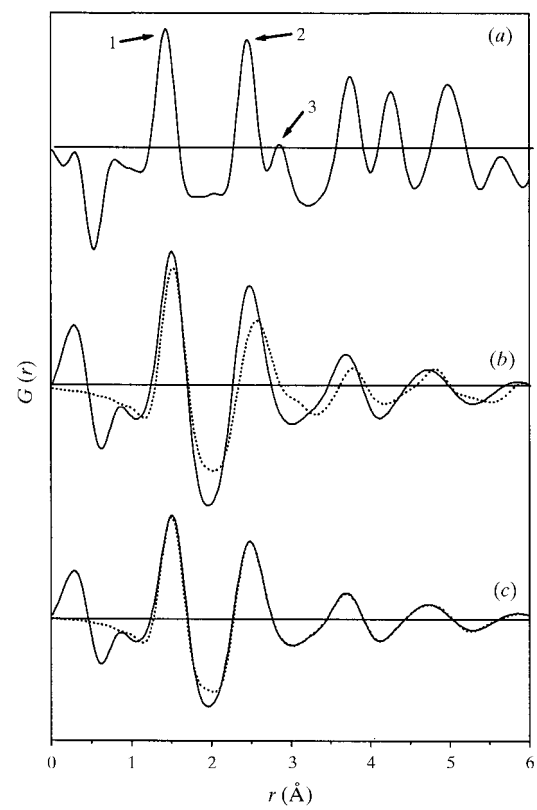

Fig. 5. (a) Reduced density functions [$G(r)$] for glassy carbon obtained from the data in Fig. 4. The numbers 1 to 3 indicate the first three nearest-neighbour distances in graphite, 1.42, 2.44 and 3.75 Å. (b) Experimental $G(r)$ for tetrahedral amorphous carbon (solid) compared with the $G(r)$ for the theoretically calculated network shown in Fig. 6 (dotted). (c) Experimental $G(r)$ for tetrahedral amorphous carbon (solid) compared with the $G(r)$ for the network shown in Fig. 6(b) (dotted).

rings were unexpected and they are absent from previous model structures proposed for tetrahedral amorphous carbon. Using this model structure, a simulated $\varphi(s)$ theory was determined using the Debye formula [equation (3)]. $\varphi(s)$ theory was then truncated at the same value of s as for the experiment, and from this $G(r)$ [dotted line in Fig. 5(*b*)] from the model structure was obtained. The nearest-neighbour distances from the experimental and the simulated $G(r)$ are shown in Table 1. The average bond angles can be calculated from the first two nearest-neighbour distances using the formula

$$\theta = 2\sin^{-1}(r_2/2r_1). \tag{6}$$

The value calculated is 115 (2)° for the simulated network compared with 111 (2)° for the experimental $G(r)$.

The simulated structure was then refined using the procedure based on the reverse Monte Carlo method described above, and the resulting structure is shown in Fig. 6(*b*). The $G(r)$ of the refined structure is compared with the experimental curve in Fig. 5(*c*) and shows excellent agreement. The refined structure (Fig. 6*b*) differs in no substantial way from the original structure (Fig. 6*a*), in that it contains the same fraction of sp^3 bonds and three- and four-membered rings. The largest atom displacement was 0.5 Å, only a fraction of a bond length, and when the energy of the refined structure was recalculated using density functional theory the increase over the value for the starting structure was only 0.1 eV atom^{-1}. We therefore conclude that the final structure is physically reasonable, and gives excellent agreement with the experimental $G(r)$.

To illustrate the difficulty in determining a unique structure from the $\varphi(s)$ or $G(r)$ data alone, we applied the same reverse Monte Carlo procedure to a different starting structure, namely a 'physically impossible' simple cubic structure. The resulting refined structure was found to produce an equally good fit of $G(r)$ to the experimental data but the final structure contained unlikely structures including five-coordinated atoms and the structure had an energy of over 1 eV atom^{-1} higher than the unrefined structure. This illustrates why it is essential to start the refinement with a reasonable model.

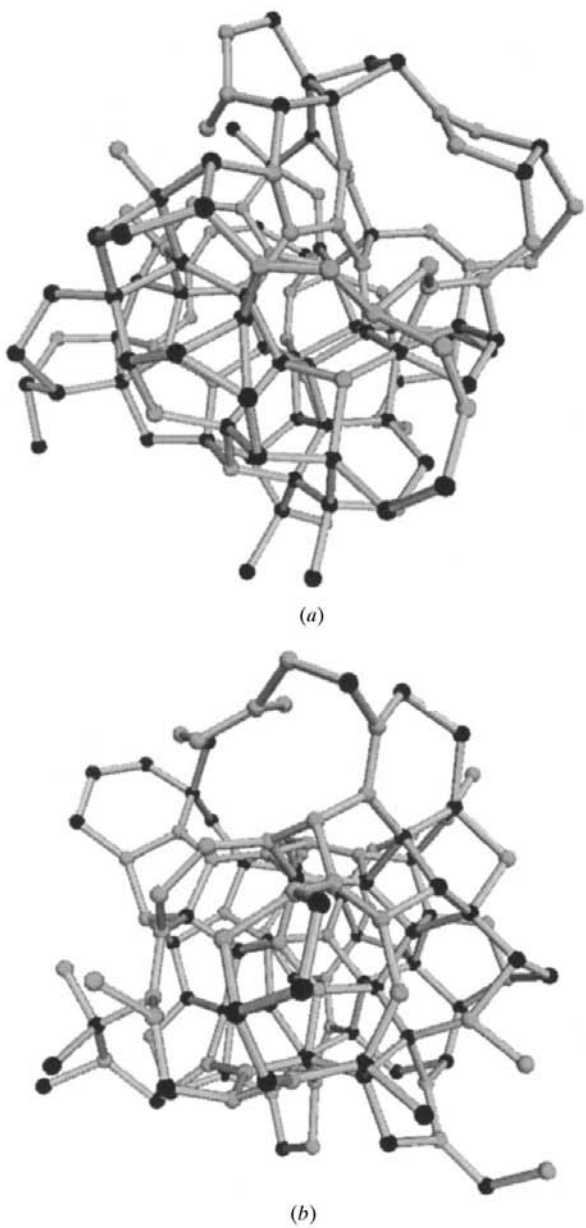

Fig. 6. (*a*) A snapshot of the 125–atom carbon network calculated using the Car–Parrinello molecular dynamics technique, and (*b*) the structure following refinement using a procedure based on the reverse Monte Carlo method. The black atoms are four-coordinated while the grey atoms are three-coordinated.

4.3. *Cathodic arc deposited aluminium nitride (AlN)*

As an example of a binary system, we now consider cathodic arc deposited AlN. The structure of crystalline AlN is a slightly distorted wurtzite structure and therefore the bond angle is expected to be close to the tetrahedral value of 109.5°. The deposition conditions affect the degree of crystallinity in AlN. Under conditions of high flux or poor thermal contact, and hence higher deposition temperature, the microstructure shows obvious signs of crystallinity, apparent as sharp rings in the diffraction pattern. Under conditions that produce more rapid quenching of the vapour and a lower deposition temperature, the diffraction pattern shows broader rings, consistent with small crystal size or an amorphous structure. This trend is apparent in Fig. 7, which shows $\varphi(s)$ for (*a*) an AlN film deposited in a cathodic arc under poor thermal contact conditions, and (*b*) an AlN film deposited in a cathodic arc under good thermal contact conditions. Figs. 8(*a*) and (*b*) show the

Table 1. *The first- and second-nearest-neighbour bond lengths and average bond angle for the experimental and theoretical systems investigated*

Material system		First-nearest-neighbour distance (Å)	Second-nearest-neighbour distance (Å)	Average bond angle (°)
Tetrahedral amorphous carbon	Experiment	1.52	2.50	115
	Model	1.52	2.56	111
	Refined model	1.52	2.50	115
Aluminium nitride	Experiment	1.90	3.16	113
	Experiment (cool)	1.90	3.14	111
	Model	1.90	3.00	104
	Refined model	1.90	3.14	111

$G(r)$ corresponding to the $\varphi(s)$ shown in Figs. 7(*a*) and (*b*), respectively. The average bond angles calculated using equation (6) are approximately 112° for both samples, only slightly larger than the expected value of 109.5°.

A snapshot of the 64-atom AlN network structure produced using the simulation outlined in §3.2 is shown in Fig. 9(*a*). During the 4000 K anneal and then the cool down to 300 K, the number of Al—N bonds in the simulated structure as a fraction of the total number of bonds (with a bond being taken to exist between any two atoms separated by less than 2.3 Å) was used as a measure of chemical ordering. This unlike-bond fraction rose rapidly from 0.25 in the initial structure to approach an asymptotic value of 1. As a random distribution of atoms would have an unlike-bond fraction of 0.5, this corresponds to a very high degree of chemical order, which is apparent in the network shown in Fig. 9(*a*).

The AlN structure may be compared with the amorphous network structure of tetrahedral amorphous carbon, however there is a much higher fraction of

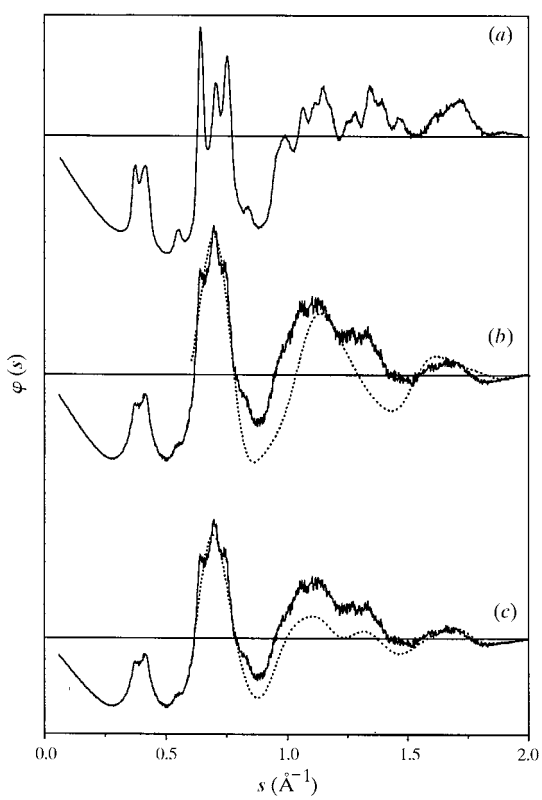

Fig. 7. (*a*) $\varphi(s)$ for cathodic arc deposited aluminium nitride deposited at high deposition temperatures. (*b*) $\varphi(s)$ for cathodic arc deposited aluminium nitride deposited at low deposition temperatures (solid) compared with the $\varphi(s)$ for the theoretically calculated network shown in Fig. 9(*a*) (dotted). (*c*) $\varphi(s)$ for cathodic arc deposited aluminium nitride deposited at low deposition temperatures (solid) compared with the $\varphi(s)$ for the network shown in Fig. 9(*b*) (dotted).

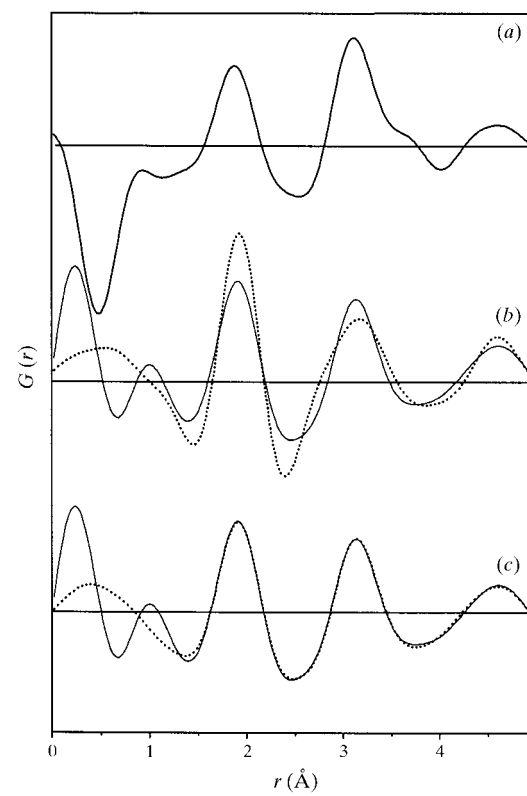

Fig. 8. (*a*) $G(r)$ for cathodic arc deposited aluminium nitride deposited at high deposition temperatures. (*b*) $G(r)$ for cathodic arc deposited aluminium nitride deposited at low deposition temperatures (solid) compared with the $G(r)$ for the theoretically calculated network shown in Fig. 9(*a*) (dotted). (*c*) $G(r)$ for cathodic arc deposited aluminium nitride deposited at low deposition temperatures (solid) compared with $G(r)$ of the theoretically calculated network shown in Fig. 9(*b*) (dotted).

tetrahedrally bonded atoms (75% in the case of AlN compared with 60% for tetrahedral amorphous carbon). In addition, we find proportionately more four-membered rings in AlN than in tetrahedral amorphous carbon because the requirement of chemical order forces the ring statistics into becoming dominated by even-membered rings. An odd-membered ring would imply a bond between two atoms of like kind. Thus, while the five-membered ring is the most common type in the tetrahedral carbon network, it is energetically unfavourable in the AlN network, forcing an increase in the number of four- and six-membered rings. This is apparent in Fig. 9(*a*). The additional constraint of chemical order causes another difference between a chemically ordered binary network and a monotonic network – the binary network appears to have larger voids in the structure; that is, its density fluctuates more on an atomic scale.

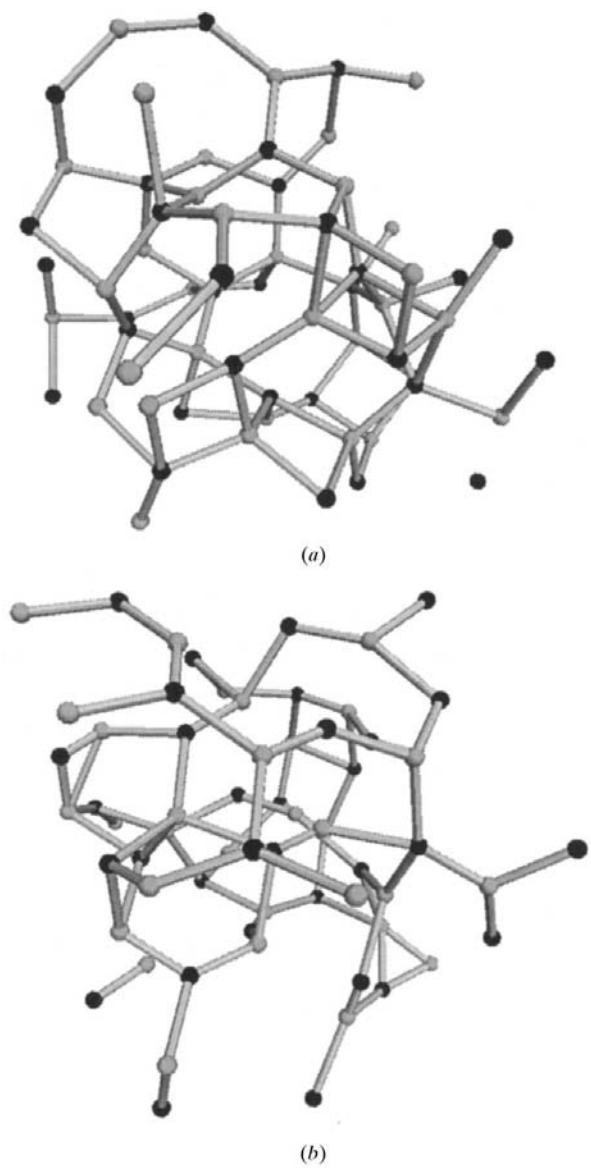

Fig. 9. (*a*) A snapshot of the 64-atom aluminium nitride network calculated using the Car–Parrinello molecular-dynamics technique. Al atoms are shown in black while N atoms are shown in grey. (*b*) The structure following refinement using a procedure based on the reverse Monte Carlo method.

$\varphi(s)$ and $G(r)$ from the calculated structure in Fig. 9(*a*) are compared with the experimental curves in Figs. 7(*b*) and 8(*b*) as dotted lines. Nearest-neighbour distances are shown in Table 1. It is clear from this comparison that $G(r)$ of the simulated structure (dotted line in Fig. 8*b*) is generally similar to the $G(r)$ obtained experimentally; however, there is a difference in the intensity of the peaks, as well as in the position of the second-nearest-neighbour peak. The comparison of experimental and theoretical $G(r)$ shows that all three structures are chemically ordered, since otherwise the Al—Al nearest-neighbour distance of ~2.86 Å would be observed in the $G(r)$.

The simulated structure was then refined using the reverse Monte Carlo method described above and the resulting structure is shown in Fig. 9(*b*). The $\varphi(s)$ and $G(r)$ of this structure are compared to experiment in Figs. 7(*c*) and 8(*c*), respectively. Although the refinement process results in an excellent agreement between experimental and theoretical $G(r)$, the sharp peaks in the experimental $\varphi(s)$ have not been reproduced. This discrepancy can be explained by the fact that the amorphous network was obtained in the simulation by using a high quench rate from the melt, whereas experimental quench rates for AlN are lower and produce a polycrystalline structure. In addition, the energy of the structure seen in Fig. 9(*b*) is over 1 eV atom^{-1} higher than the structure prior to the refinement. This points to an important difference between the AlN and tetrahedral amorphous carbon examples. In the AlN case, we are trying to fit experimental data for a polycrystalline specimen with an amorphous network structure. By means of the reverse Monte Carlo procedure alone, the structure is not able to organize itself into a crystalline structure of low entropy by essentially random movements. For this reason, the refinement procedure has not been successful in finding the correct structure, *i.e.* the structure that provides the best fit to the experiment and of low energy. Although there is a probability of finding the correct structure, it is vanishingly small. Therefore, we recommend caution when using this procedure to determine structure in polycrystalline materials.

5. Conclusions

Refinements in technique now allow the rapid collection of the scattered intensity $I(s, \Delta E)$ over a range of s and ΔE. The interpretation of the data for elastic scattering from disordered or network solids is greatly assisted by

the ability to obtain realistic predictions of structure. First-principles methods of molecular dynamics based on the density functional theory of quantum mechanics provide an excellent starting point for finding structural models. The refinement of these models using reverse Monte Carlo methods can be effective but are reliable only when accompanied by calculations of the energy of the structure. The power of the technique is illustrated by its application to tetrahedral amorphous carbon. An attempt to find a structural model for a polycrystalline sample of AlN using this method did not succeed owing to the vanishingly small probability that an amorphous structure will crystallize by random movements alone.

References

Aksenov, I. I., Belous, V. A., Padalka, V. G. & Khoroshikh, V. M. (1978). *Fiz. Plazmy*, **4**, 758–763.

Becke, A. D. (1988). *Phys. Rev. A*, **38**, 3098–3100.

Berger, S. D., McKenzie, D. R. & Martin, P. J. (1988). *Philos. Mag. Lett.* **57**, 285–290.

Car, R. & Parrinello, M. (1985). *Phys. Rev. Lett.* **55**, 2471–2474

Cobb, M., Cappelletti, R. L. & Drabold, D. A. (1996). *Phys. Rev. B*, **54**, 12161–12171.

Cockayne, D., Mckenzie, D. & Muller, D. (1991). *Microsc. Microanal. Microstruct.* **2**, 359–366.

Cockayne, D. J. H. & McKenzie, D. R. (1988). *Acta Cryst.* A**44**, 870–878.

Doyle, P. A. & Turner, P. S. (1968). *Acta Cryst.* A**24**, 390–397.

Egerton, R. F. (1996). *Electron Energy Loss Spectroscopy in the Electron Microscope.* New York: Plenum Press.

Evans, R. A. (1990). *Mol. Simul.* **4**, 409–411.

Graczyk, J. F. & Moss, S. C. (1969). *Rev. Sci. Instrum.* **40**, 424–433.

Grigson, C. W. B. (1962). *J. Electron Spectrosc.* **12**, 209–216.

Hohenberg, P. & Kohn, W. (1964). *Phys. Rev.* **136**, B864–B871.

Hoover, W. G. (1985). *Phys. Rev. A*, **31**, 1695–1697.

Hutter, J., Carloni, P. & Parrinello, M. (1996). *J. Am. Chem. Soc.* **118**, 8710–8712.

Jenkins, G. M. & Kawamura, K. (1976). *Polymeric C atoms – Carbon Fibre Glass and Char.* Cambridge University Press.

Kohn, W. & Sham, L. J. (1965). *Phys. Rev.* **140**, A1133–A1138.

Lee, C., Yang, W. & Parr, R. G. (1988). *Phys. Rev. B*, **37**, 785–789.

McBride, W., McCulloch, D. G., McKenzie, D. R. & Green, D. (1998). *Micron*, **29**, 1–5.

McGreevy, R. L. & Howe, M. A. (1992). *RMC: Modeling Disordered Structures. Annual Review of Materials Science*, pp. 217–242.

McKenzie, D. R., Davis, C. A., Cockayne, D. J. H., Muller, D. A. & Vassallo, A. M. (1992). *Nature (London)*, **355**, 733–734.

McKenzie, D. R., Green, D. C., Swift, P. D., Cockayne, D. J. H., Martin, P. J., Netterfield, R. P. & Sainty, W. G. (1990). *Thin Solid Films*, **193/194**, 418–430.

McKenzie, D. R., Muller, D. & Pailthorpe, B. A. (1991). *Phys. Rev. Lett.* **67**, 773–776.

McKenzie, D. R., Sainty, W. G. & Green, D. (1990). *Mater. Sci. Forum*, **54/55**, 193–206.

Marks, N. A., McKenzie, D. R., Pailthorpe, B. A., Bernasconi, M. & Parrinello, M. (1996). *Phys. Rev. Lett.* **76**, 768–771.

Merchant, A. R., McCulloch, D. G., McKenzie, D. R., Yin, Y., Hall, L. & Gerstner, E. G. (1996). *J. Appl. Phys.* 79, 6914–6919.

Nose, S. (1984). *Mol. Phys.* **52**, 255–268.

Sarnthein, J., Pasquarello, A. & Car, R. (1995). *Phys. Rev. B*, **52**, 12690–12695

Sproul, A., McKenzie, D. R. & Cockayne, D. J. H. (1986). *Philos. Mag.* B**54**, 113–131.